THE JOURNAL OF PHYSICAL CHEMISTRY A
A JOURNAL OF THE AMERICAN CHEMICAL SOCIETY

pubs.acs.org/JPCA

Article

The N^+ Formation Mechanism of Vibrationally Selected N_2O^+ Ions in the $C^2\Sigma^+$ State: A TPEPICO Imaging Study

Published as part of The Journal of Physical Chemistry A virtual special issue "Xueming Yang Festschrift".

Yan Chen, Xiangkun Wu, Xiaoguo Zhou,* Xinlang Yang, Xinhua Dai,* and Shilin Liu*

Cite This: *J. Phys. Chem. A* 2024, 128, 4439−4447

Read Online

ACCESS | Metrics & More | Article Recommendations | Supporting Information

ABSTRACT: The N−NO bond fission of $N_2O^+(C^2\Sigma^+)$ ions can produce two major fragment ions, NO^+ or N^+. In contrast to the dominant NO^+ fragment ion, the N^+ formation mechanism remains unclear to date. Here, dissociative photoionization of N_2O via the $C^2\Sigma^+$ ionic state has been reinvestigated using a combined approach of threshold photoelectron−photoion coincidence (TPEPICO) velocity imaging and quantum chemical calculations. Accompanying the $N^+(^3P)$ formation, the $NO(X^2\Pi)$ neutral fragment with low and high vi-rotational distributions was identified, based on the N^+ speed and angular distributions derived from the TPEPICO images. In particular, the excitation of the symmetric stretching ν_1^+ mode promotes the formation of high rotational components, while the asymmetric stretching ν_3^+ mode shows the exact opposite effect. According to our calculated multistate potential energy surfaces, intersystem crossing from $C^2\Sigma^+$ to $1^4\Pi$ exclusively provides feasible decomposition pathways to produce the N^+ fragment. In a slightly bent geometry, spin−orbit couplings between $C^2\Sigma^+$ and two substates of $1^4\Pi$, $1^4A'$ or $1^4A''$, play a crucial role in the N^+ formation from vibrationally selected $N_2O^+(C^2\Sigma^+)$ ions. The mechanism also provides new insights into the charge transfer reaction of $N^+ + NO \rightarrow N + NO^+$.

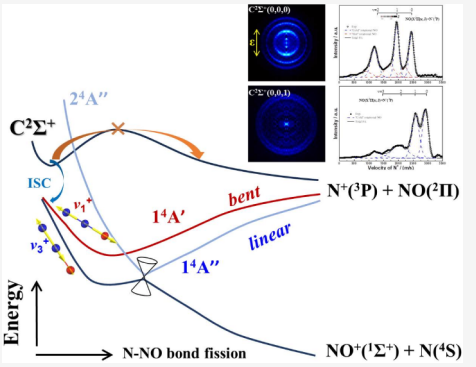

Downloaded via UNIV SCIENCE AND TECHNOLOGY CHINA on June 7, 2024 at 02:10:27 (UTC).
See https://pubs.acs.org/sharingguidelines for options on how to legitimately share published articles.

1. INTRODUCTION

Nitrous oxide (N_2O), one of the most dominant long-lived greenhouse gases with a 116 ± 9 years[1] atmospheric lifespan, has seen a notable increase in emissions due to agricultural practices and N-fertilizer use, significantly impacting global warming.[2−4] Additionally, in the stratosphere, crucial processes such as photodissociation and dissociative photoionization of N_2O can release reactive substances such as O and NO radicals, which deplete stratospheric ozone.[5] Therefore, studying the dissociative photoionization of N_2O can provide fundamental data and offer essential insights for atmospheric science. These topics have attracted extensive attention during past decades.[6−13]

Both direct and indirect dissociation mechanisms have been verified in the decomposition process of N_2O^+ in low-lying electronic states, due to complex and diverse interactions. The $A^2\Sigma^+$, $B^2\Pi$, $C^2\Sigma^+$, and $D^2\Pi$ states of N_2O^+ are all predissociative, except for a few lowest vibronic levels of $A^2\Sigma^+$.[9−11,13−15] In the decomposition of $N_2O^+(A^2\Sigma^+)$ ions, NO^+ fragment was distinctly observed with bimodal rotational distributions along the $NO^+(X^1\Sigma^+) + N(^2D)$ pathway, besides the lowest one of $NO^+(X^1\Sigma^+) + N(^4S)$.[13] Likewise, the $NO^+(X^1\Sigma^+) + N(^2D)$ pathway also dominated in the decomposition of $N_2O^+(B^2\Pi)$ ions, and the molecular bending was suggested to occur prior to the dissociation.[9,16] Very recently, we have conducted high-level *ab initio* calculations on N_2O^+ in the $A^2\Sigma^+$ and $B^2\Pi$ states, using the complete active space self-consistent field (CASSCF) and multireference second-order perturbation theory (CASPT2).[17] By mapping two-dimensional (2D) multistate potential energy surfaces along the N−NO bond length and N−N−O angle, we have proposed comprehensive N−NO bond-fission mechanisms in linear and bent geometries to explain ro-vibrational distributions of the NO^+ fragment observed in experiments, in which the avoided crossing and the coupling of spin states play crucial roles.[17]

The decomposition of $N_2O^+(C^2\Sigma^+)$ ions is more complex, and many dissociation channels are open owing to the increase of excitation energy and multistate coupling.[18,19] Four fragment ions, NO^+, N_2^+, O^+, or N^+, were all observed in experiments, and their branching ratios exhibited some degree of vibrational dependence.[19−21] By fitting the TOF profile of the dominant NO^+ fragment, Nenner et al.[19] and Chiang and Ma[21] independently obtained average kinetic energy release distributions (KERDs). Their results consistently showed a vibrational dependence, which was roughly attributed to the

Received: January 24, 2024
Revised: May 16, 2024
Accepted: May 16, 2024
Published: May 23, 2024

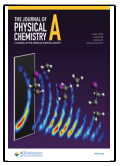

© 2024 American Chemical Society

https://doi.org/10.1021/acs.jpca.4c00494
J. Phys. Chem. A 2024, 128, 4439−4447

effect of vibrational energy on the multistate coupling dissociation via the $^2\Pi$ state.[21] Furthermore, Lebech et al.[22] measured the molecular-frame photoelectron angular distribution in the photoionization to $C^2\Sigma^+$ using electron−ion velocity vector correlation, and a lifetime of ∼2 ps was obtained for $C^2\Sigma^+$ with the aid of multichannel Schwinger configuration interaction calculations. In 2011, we investigated the NO^+ formation mechanism of $N_2O^+(C^2\Sigma^+)$ using threshold photoelectron−photoion coincidence (TPEPICO) velocity imaging.[11] The excited asymmetric stretching (ν_3^+) was found to effectively promote the branching ratio of the $NO^+(X^1\Sigma^+)$ + $N(^2D)$ pathway. In contrast, the other product channel of the N−NO bond-fission of $N_2O^+(C^2\Sigma^+)$, N^+ + NO, is rarely mentioned. Although a vibrational dependence of the N^+ branching ratio in the dissociative photoionization of N_2O was also observed,[11,20,21,23] the KERD and angular distribution of the fragments, as well as the corresponding formation mechanism, remain unknown. In addition, N_2O^+ has been observed as the intermediate of the ion-molecular reaction of $O^+(^4S)$ + N_2 in the ionospheres of Earth, Mars, and Venus,[6,24] from which the electron-transfer reaction of N^+ + NO → NO^+ + N can be initiated.[25] Considering that the appearance energies of NO^+ + N and N^+ + NO are 14.19 eV[19] and 19.46 eV,[19,26] respectively, this electron-transfer reaction occurs at least in the energy range of $C^2\Sigma^+$ ionic state according to its ionization energy of 20.100 eV.[11] It motivates us to investigate the N^+ formation mechanism in dissociative photoionization of N_2O toward the $C^2\Sigma^+$ ionic state using a combined approach of state-of-the-art TPEPICO velocity map imaging and high-level quantum chemical calculations, which have been successfully applied on dissociation dynamics of energy-selected ions in the gas phase as one of the most powerful approaches.[27]

In this work, an experimental reinvestigation on dissociative photoionization of N_2O in the photon energy range of 20.0−20.8 eV is carried out using TPEPICO velocity imaging. Thanks to the high energy resolution of imaging ($\Delta E/E$ ∼ 2%), both speed and angular distributions of the N^+ fragment are distinctly obtained. To understand the vibrationally mediated photodissociation dynamics, various vibrational modes of $N_2O^+(C^2\Sigma^+)$ ions are excited, and the results are compared with each other. Moreover, multistate potential energy surfaces of N_2O^+ in $C^2\Sigma^+$ and nearby quartet states are calculated using CASSCF and CASPT2 approaches. Combining the experimental and theoretical results, we reveal that the N^+ formation mechanism from $N_2O^+(C^2\Sigma^+)$ ions. The vibrational dependence of energy distributions of fragments is discussed with the aid of vibrational mode analyses, and the interaction between the $C^2\Sigma^+$ and $1^4\Pi$ states is proposed to play a vital role in the vibrationally mediated dissociation dynamics of $N_2O^+(C^2\Sigma^+)$ ions.

2. EXPERIMENTAL AND COMPUTATIONAL METHODS

The dissociative photoionization experiments were performed at the BL09U undulator beamline of the National Synchrotron Radiation Laboratory (Hefei, China). The details of the TPEPICO velocity imaging spectrometer[28] and the beamline[29] have been described previously, and thus only a brief introduction is outlined here. Figure S1 shows a schematic diagram of this apparatus. Vacuum ultraviolet (VUV) photons from an undulator of the 800 MeV electron-storage ring were collimated and dispersed by a monochromator with a 370-lines/mm grating and then focused into a differentially pumped gas filter filled with helium for suppressing higher-order radiations. In current experiments, the entrance and exit slits of the monochromator were set at 80 μm, corresponding to the energy resolution power ($E/\Delta E$) of ∼2000 at 15 eV.[29] The absolute photon energy was calibrated using well-known autoionization lines of argon and neon. A silicon photodiode (International Radiation Detectors, SXUV-100) was used to record photon flux for normalization of the threshold photoelectron spectra (TPES).

Commercial N_2O gas (99.9% purity) with a stagnation pressure of 2.8 atm was injected into a vacuum chamber through a 30-μm-diameter nozzle to form a supersonic molecular beam. By collimating by a 0.5 mm-diameter skimmer, the molecular beam was introduced into the photoionization chamber and intersected with the VUV photons at 10 cm downstream from the nozzle. The typical backing pressures of the source and ionization chambers were less than 1×10^{-5} Pa, while they were increased to 6×10^{-3} Pa and 1×10^{-4} Pa with the molecular beam on. The produced electrons and ions were extracted and velocity-mapped in opposite directions by a DC extraction field of 14 V/cm. A 1 mm-diameter aperture mask was placed in front of the electron detector, only allowing threshold electrons to pass through. Due to the effect of the magnified ion optics for electrons, hot electron contamination can be efficiently suppressed. The TPEPICO measurements were performed with the single-start−multiple-stop data acquisition mode,[30] in which electrons were used to trigger TOF measurements of ions. The coincident ions were projected onto dual MCPs backed by a phosphor screen (Burle Industries, P43), and the images on the screen were recorded with a thermoelectric-cooling CCD camera (Andor, DU934N-BV). In experiments, a pulsed high voltage was applied at the MCPs as a mass gate (duration of 60 ns) to achieve three-dimensional (3D) time-sliced velocity images of the specific ions.

To theoretically study the dissociation mechanisms of $N_2O^+(C^2\Sigma^+)$ ions, quantum chemical calculations were performed using the MOLPRO version 2021.3 program.[31] The molecular geometry of $N_2O^+(C^2\Sigma^+)$ was optimized at the CASPT2/cc-pVQZ level, and the corresponding excitation energies were calculated for mapping multistate potential energy surfaces of the lowest several doublet and quartet states at the CASSCF/cc-pVQZ level. As the N−O bond length almost remains in the dissociative photoionization process in the current excitation energy range, only 2D potential energy surfaces were paid attention to along the N−NO bond length and the N−N−O angle, while the N−O bond length was fixed at 1.209 Å. Based on the CASSCF wave functions, the full valence active space including the $4\sigma-9\sigma$ and $1\pi-3\pi$ orbitals was chosen, and 15 electrons for cations were active, i.e., CASSCF(15,12) for N_2O^+. In addition, vibrational frequency analyses of $N_2O^+(C^2\Sigma^+)$ were carried out at the TD-B3LYP/6-311G+(d) level using the Gaussian 16 program.[32]

3. RESULTS AND DISCUSSION

3.1. TPES and Fragmentation of $N_2O^+(C^2\Sigma^+)$. As shown in the previous TPES of N_2O in the photon energy range of 20.0−20.8 eV (also shown in Figure S2),[11] three dominant vibrational peaks, located at 20.100, 20.260, and 20.390 eV, are attributed to the photoionization transitions from the vibrational ground state of neutral $N_2O(X^1\Sigma^+)$ to the (0,0,0), (1,0,0), and (0,0,1) vibronic levels of $N_2O^+(C^2\Sigma^+)$, where the

https://doi.org/10.1021/acs.jpca.4c00494
J. Phys. Chem. A 2024, 128, 4439−4447

numbers in parentheses represent vibrational quanta for the ν_1^+ (symmetric stretch), ν_2^+ (bending), and ν_3^+ (asymmetric stretch) modes, respectively. The most intense (0,0,0) band, together with very weak bending peaks, indicates a quasilinear geometry of $N_2O^+(C^2\Sigma^+)$ in the Franck−Condon region.[18,19,33]

Once the $N_2O^+(C^2\Sigma^+)$ ions are formed, the molecular ions will fully dissociate into fragment ions. In our previous study,[11] a bimodal vibrational distribution was observed for the NO^+ fragment, corresponding to the $NO^+(X^1\Sigma^+)$ + $N(^2P)$ and $NO^+(X^1\Sigma^+)$ + $N(^2D)$ dissociation pathways. In comparison to the NO^+ formation pathway, N^+ accounted for approximately 10% of the fragment abundance in the dissociation of $C^2\Sigma^+(0,0,0)$ and (1,0,0), while it was increased to 20% for $C^2\Sigma^+(0,0,1)$. In other words, excitation of the ν_3^+ vibrational mode can efficiently promote the N−NO bond fission to produce N^+ rather than NO^+. Moreover, as shown in Figure 1,

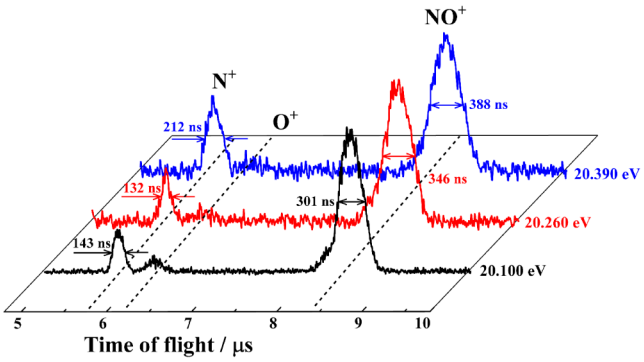

Figure 1. Vibrational state-selected TPEPICO TOF mass spectra for the dissociative photoionization of N_2O at 20.100, 20.260, and 20.390 eV.

the N^+ TOF width (FWHM) is slightly changed from 143 ns at the (0,0,0) vibronic level to 132 ns at (1,0,0) and 212 ns at (0,0,1), and the corresponding TOF profiles exhibit minor changes; for example, the (1,0,0) distribution is closer to a Gauss-type shape. These evidences imply vibrational dependence of the N−NO bond-breaking mechanism of $N_2O^+(C^2\Sigma^+)$ ions.

3.2. TPEPICO Velocity Images of the N^+ Fragment. In order to compare more clearly the differences of energy distribution in the N^+ formation from different vibrational states of $C^2\Sigma^+$, the TPEPICO velocity images of N^+ were recorded at 20.100, 20.260, and 20.390 eV. Considering that the false-coincident signals always exist in the originally recorded images in TPEPICO measurements, true images of target fragment ions are obtained after a data processing process,[34] in which the subtraction of false coincidence images and deconvolution and quadrant symmetrization are sequentially performed. Figure 2 shows the modified 3D time-sliced velocity map images of the N^+ fragment ion, while the raw images and data processing are exhibited in Figure S3. In the current experiments, the molecular beam flowed along the *y*-axis direction from bottom up, and the electric field vector ε of the VUV photons also propagated along the *y*-axis in this configuration. Frankly, the residual contributions of the false coincidence ions are still observed in all the images of Figure 2 as the symmetrical top and bottom spots close to the center due to the nonuniformity of measurements of coincidence and

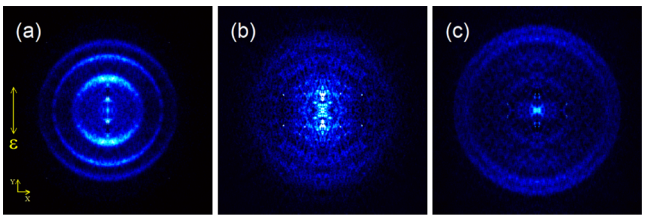

Figure 2. 3D time-sliced coincidence images of N^+ dissociated from the N_2O^+ $(C^2\Sigma^+)$ ions in (a) the (0,0,0) level at 20.100 eV, (b) the (1,0,0) level at 20.260 eV, and (c) the (0,0,1) level at 20.390 eV.

false coincidence ions, despite the fact that we have already adopted the deduction.

Although the signal-to-noise ratio of Figure 2b is barely satisfactory, similar image patterns can be observed for the (0,0,0) and (1,0,0) levels. In Figure 2a,b, three major homocentric rings are distinctly observed with a certain degree of anisotropy. Obviously, these rings correspond to vibrational excitations of the NO neutral fragment. Actually, the similarity was also observed previously in the images of the NO^+ fragment.[11] To our surprise, the N^+ image recorded at the (0,0,1) level shows totally different patterns from the other ones. As shown in Figure 2c, two distinct outer rings and a fuzzy inner ring are visible.

By accumulating the intensity of the image over all angles, the speed distribution of the N^+ fragment was obtained and plotted in Figure 3. In the current photon energy range, the $N^+(^3P)$ + $NO(X^2\Pi)$ decomposition pathway is the unique one that is energetically feasible for the N^+ formation.[11,18,19] According to the active thermochemical tables (ATcTs),[19,26] the corresponding dissociation limit D_0 equals 19.46 eV. Taking into account the vibrational frequency (1876 cm^{-1})[35,36] and the rotational constant (1.6961 cm^{-1})[37] of the neutral $NO(X^2\Pi)$, the ro-vibrational population of the NO fragment dissociated from the three vibrational states of $N_2O^+(C^2\Sigma^+)$ was calculated and marked in Figure 3.

As shown in Figure 3a, three discrete peak centers are very close to three vibrational levels (v = 0−2) of NO, indicative of the low rotational excitation. For example, the most dominant rotational distribution is located at J < 5 for the v = 1 level. Moreover, an inversion of vibrational population is observed. As shown in the assignments in Figure 3a, the maximum vibrational population of the NO fragment is located at v = 1. Thus, the N^+ formation in the decomposition of N_2O^+ ions in the (0,0,0) level of $C^2\Sigma^+$ is typically nonstatistical. Additionally, there are some distributions between the three dominant peaks, as shown in Figure 3a. Obviously, these minor components can be attributed to the high rotational distributions of NO in the corresponding vibrational states with the center at J ∼ 24. Interestingly, the maximal intensity of the "hot" rotational component is also located at v = 1, in line with the "cold" one. This implies that both "cold" and "hot" rotational components might undergo the same intermediate state prior to the N−NO bond fission.

For the dissociation of $N_2O^+(C^2\Sigma^+)$ ions in the (1,0,0) level, the poor quality of the image seriously affects the accuracy of the speed distribution. In this matter, it was reluctantly fitted using two series of peaks, as exhibited in Figure 3b, corresponding to the two N^+ formation pathways in the N−NO bond-breaking process. Although the population pattern is generally consistent with that of the (0,0,0) level, there are still some visible changes between Figure 3a and 3b. Due to the

https://doi.org/10.1021/acs.jpca.4c00494
J. Phys. Chem. A 2024, 128, 4439−4447

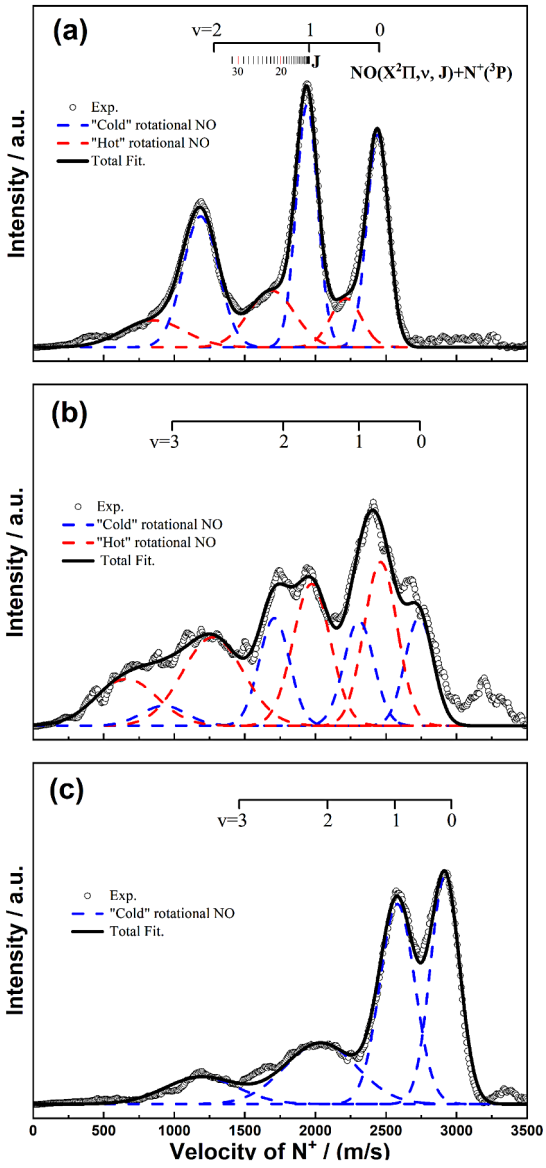

Figure 3. Speed distributions of the N^+ fragment dissociated from $N_2O^+(C^2\Sigma^+)$ ions at the (0,0,0) (a), (1,0,0) (b), and (0,0,1) (c) levels. The dots are the experimental distributions derived from the images in Figure 2, while the solid lines represent the multipeak fitting results in terms of Gaussian profiles. The blue and red dashed lines are the NO components with low and high rotational excitations, respectively.

higher available energy prior to dissociation, the vibrational population of the NO fragment is expanded to v = 3 in the dissociation of $C^2\Sigma^+(1,0,0)$. Moreover, in comparison to the (0,0,0) result, the excitation of the ν_1^+ mode significantly promotes the contribution of the high rotational component, as shown in Figure 3b.

In contrast, the N^+ speed distribution in the (0,0,1) level has changed dramatically (Figure 3c). A satisfactory fitting can be achieved using only one series of vibrational peaks, whose centers generally correspond to the vibronic levels (v = 0−3) of NO. This strongly indicates that the neutral NO fragment in low rotational states predominates for the decomposition of $C^2\Sigma^+(0,0,1)$, while the channel to produce the "hot" rotational NO fragment is negligible. In addition, the populations of the v = 2 and 3 states are significantly reduced in comparison to those of the lower vibrational states, and moreover, the corresponding widths are remarkably increased. Such mutations usually indicate the change of dissociation mechanism.

To demonstrate the above changes more clearly, we calculated the relative branching ratios of the "hot" and "cold" rotational components by integrating their population intensities and listed the results in Table 1. Obviously, the

Table 1. Branching Ratios of the NO Fragment with the "Cold" and "Hot" Rotational Excitations in the Decomposition of $N_2O^+(C^2\Sigma^+)$ Ions

vibronic levels	branching ratio	
	"cold" rotational	"hot" rotational
(0, 0, 0)	71% ± 4%	29% ±4%
(1, 0, 0)	35% ± 8%	65% ± 8%
(0, 0, 1)	95%	<5%

excitation of various vibrational modes exhibits significant influences on the rotational populations of the neutral NO fragment. For example, the branching ratio of the low rotational component is decreased from 71% to 35% when the ν_1^+ mode is excited, but it is improved to more than 95% with the excitation of ν_3^+. Thus, the branching ratio does not show an inconsistent trend with internal energies, implying that the unimolecular decomposition is nonstatistical, and the excitation of ν_1^+ and ν_3^+ modes might lead to different indirect dissociation pathways. Notably, the similar dependence on the vibrational modes was also observed for the other N−NO bond rupture pathway of $N_2O^+(C^2\Sigma^+)$ ions, i.e., the NO^+ formation,[11] in which the excited ν_3^+ mode could improve the branching ratio of the $NO^+(X^1\Sigma^+)$ + $N(^2D)$ pathway. We will further discuss this effect in Section 3.6, with the aid of quantum chemical calculations.

3.3. Energy and Angular Distributions in the Decomposition of $N_2O^+(C^2\Sigma^+)$ Ions. Based on the above speed distributions, the proportion of average total kinetic energy ⟨TKE⟩ and available energy E_{avail} (= $h\nu - D_0$) in the molecular dissociation was calculated as $f_T = \frac{\langle TKE\rangle}{E_{avail}}$. The results for N^+ formation in the decomposition of $N_2O^+(C^2\Sigma^+)$ ions at various vibrational states are listed in Table 2. It is well-known that, for the rapid dissociation of a triatomic molecule, the classical "impulsive model"[38] is usually expected to describe its mechanism, in which the f_T value can be expressed as $f_T = \frac{\langle TKE\rangle}{E_{avail}} = \frac{\mu_{N-N}}{\mu_{N-NO}} = 0.733$, where μ is the corresponding reduced mass. In this circumstance, the N−NO bond of N_2O^+ ions is broken at a specific bond angle in such a short period of time that intramolecular vibrational redistribution (IVR) cannot happen in time, and the oxygen atom plays the role of a spectator. Using the mean vibrational and rotational energies of the NO fragment, $\langle E_{vib}\rangle$ and $\langle E_{rot}\rangle$, we can calculate the bond angle χ at the moment of dissociation with the following formulas (eqs 1 and 2):

$$\langle E_{vib}\rangle = (1 - f_T)\cdot E_{avail}\cdot\cos^2\chi \quad (1)$$

$$\langle E_{rot}\rangle = (1 - f_T)\cdot E_{avail}\cdot\sin^2\chi \quad (2)$$

As shown in Table 2, an obvious difference exists between the f_T values of the high and low rotational components. In general, the f_T value of the low rotational component is consistently larger than that of the high rotational one,

https://doi.org/10.1021/acs.jpca.4c00494
J. Phys. Chem. A 2024, 128, 4439−4447

Table 2. Energy Distributions of the N^+ Fragment Dissociated from $N_2O^+(C^2\Sigma^+)$ Ions in Various Vibrational States

vibronic levels	$h\nu$/eV	E_{avail}	⟨TKE⟩/eV			f_T		
			expt.	"cold"	"hot"	expt.	"cold"	"hot"
(0,0,0)	20.100	0.64	0.37	0.40	0.32	0.61	0.62	0.50
(1,0,0)	20.260	0.80	0.43	0.54	0.41	0.54	0.68	0.51
(0,0,1)	20.390	0.93	0.66	0.69	-	0.71	0.74	-

regardless of vibrational states, indicating the faster dissociation rate of N_2O^+ ions along the quasi-linear geometry than the bent one. Moreover, for the low rotational component, the f_T values gradually increase with available energy. Especially, the experimental value of f_T (= 0.71) at the (0,0,1) level is extremely close to the impulsive limit (0.733). In addition, in the dissociation of $C^2\Sigma^+(1,0,0)$, $\langle E_{vib}\rangle$ and $\langle E_{rot}\rangle$ of the high rotational ("hot") component are 0.30 and 0.09 eV, respectively. Thus, the bond angle χ at the moment of dissociation using the "impulsive model" is determined to be 151°, according to eqs 1 and 2.

In addition to the energy distributions, angular distributions of the N^+ fragment can also be derived from the images. By integration of the intensities over a specific speed range (usually half-width of the fitted peak) at each angle, the angular distribution of the N^+ fragment dissociated from the vibrationally selected $N_2O^+(C^2\Sigma^+)$ ions is obtained and shown in Figures S4–S6. Subsequently, the anisotropy parameter β is achieved by fitting the angular distribution, $I(\theta)$, with the formula,[39] $I(\theta) = \frac{1}{4\pi}[1 + \beta \cdot P_2(\cos\theta)]$, where θ is the angle between the recoil velocity of fragment, and the electric field vector ε of the VUV photon, and $P_2(\cos\theta)$ is the second-order Legendre polynomial. It is well-known that a statistical dissociation usually has an isotropic angular distribution with $\beta = 0$, while a nonstatistical dissociation shows a nonzero β value, e.g., $\beta = 2$ for parallel and $\beta = -1$ for perpendicular distributions.

Since the "hot" rotational component has minor contributions in the images of Figure 2, especially for the (0,0,0) and (0,0,1) levels, Table 3 summarizes only the fitted β values of the N^+ fragment with the "cold" rotational distribution. The β values all are larger than zero, indicating a parallel dissociation tendency for the decomposition of $N_2O^+(C^2\Sigma^+)$. We would like to emphasize that these β values are very close to the reported data for the formation of NO^+ dissociated from $N_2O^+(C^2\Sigma^+)$.[11] This consistency greatly agrees with the $N_2O^+(C^2\Sigma^+)$ lifetime being shorter than the rotational period. Moreover, with the vibrational quanta (v) of the neutral NO fragment increasing, the β value is slightly reduced for each specific vibrational state of the $N_2O^+(C^2\Sigma^+)$ ions, as indicated in Table 3. For the NO fragment in the same vibronic level, the vibrational excitation of parent ions reduces the corresponding β value, e.g., β = 0.91 at (0,0,0), 0.58 at (1,0,0) and 0.67 at (0,0,1) for the NO (v = 0) fragmentation. The decreased tendency of the β value with vibrational excitation indicates some potential changes in the dissociation mechanism of $N_2O^+(C^2\Sigma^+)$ ions when the vibrational stretching modes are excited.

Table 3. Anisotropy Parameters β of the N^+ Fragment Corresponding to the Low Rotationally Excited NO in the Decomposition of $N_2O^+(C^2\Sigma^+)$ Ions at the (0,0,0), (1,0,0), and (0,0,1) VibronicLevels

vibronic levels	anisotropy parameter, β[a]			
	v = 0	v = 1	v = 2	v = 3
(0,0,0)	0.91 ± 0.08	0.91 ± 0.06	0.80 ± 0.05	-
(1,0,0)	0.58 ± 0.12	0.40 ± 0.17	0.39 ± 0.15	0.23 ± 0.11
(0,0,1)	0.67 ± 0.07	0.65 ± 0.08	0.54 ± 0.09	0.30 ± 0.10

[a]v is the vibrational quanta of the corresponding neutral NO fragment.

3.4. Optimized Geometry and Potential Energy Surface of $N_2O^+(C^2\Sigma^+)$. To clearly understand the dissociation characteristics of the $C^2\Sigma^+$ state, we performed high-level quantum chemical calculations on its optimized geometry and mapped 2D potential energy surface along the N–NO coordinate and bond angle at the CASPT2//cc-pVQZ level, similar to our recent calculations of the $A^2\Sigma^+$ and $B^2\Pi$ states.[17] In the Franck–Condon region, a linear optimized geometry is affirmed for the $C^2\Sigma^+$ state with R(N–N) of 1.119 Å and R(N–O) of 1.209 Å. These bond lengths are close to those of $A^2\Sigma^+$ state, in line with their similar spectral patterns in TPES.[19,33] Moreover, vertical ionization energy (VIE) and adiabatic ionization energy (AIE) of $C^2\Sigma^+$ are calculated to be 19.89 and 19.77 eV, respectively, which reasonably agree with the experimental values, 20.11, 20.10, and 20.101 ± 0.007 eV.[11,19,21]

Figure 4 shows the calculated 2D potential energy surface of the $C^2\Sigma^+$ state along the N–NO coordinate and bond angle.

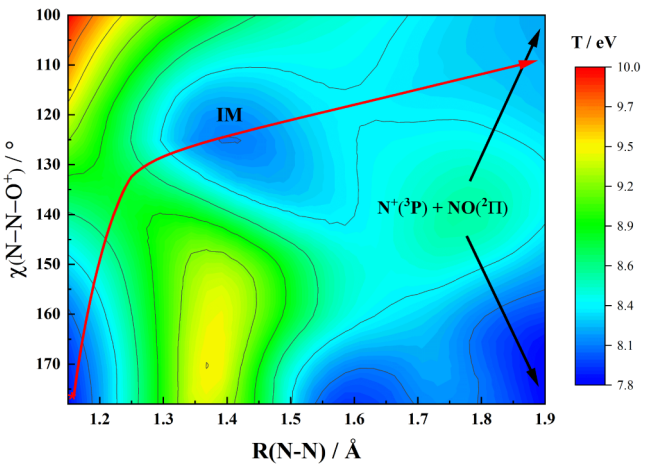

Figure 4. CASSCF potential energy surface of the $C^2\Sigma^+(^2A')$ state for N_2O^+ along the N–NO bond length and the N–N–O angle, in which the N–O bond length of N_2O^+ is fixed at 1.209 Å. The red curve shows the minimum energy path.

Notably, the pattern is generally similar to those of the lower excited states, $A^2\Sigma^+$ and B^2A' (the A′ component of $B^2\Pi$ in bent geometry).[17] In brief, from the global minimum of the $C^2\Sigma^+$ state (linear geometry) in the Franck–Condon region, a relatively high barrier of ~1.8 eV exists to break the N–NO bond of $N_2O^+(C^2\Sigma^+)$ along the linear configuration. Alternatively, as shown by the minimum energy path with

https://doi.org/10.1021/acs.jpca.4c00494
J. Phys. Chem. A 2024, 128, 4439–4447

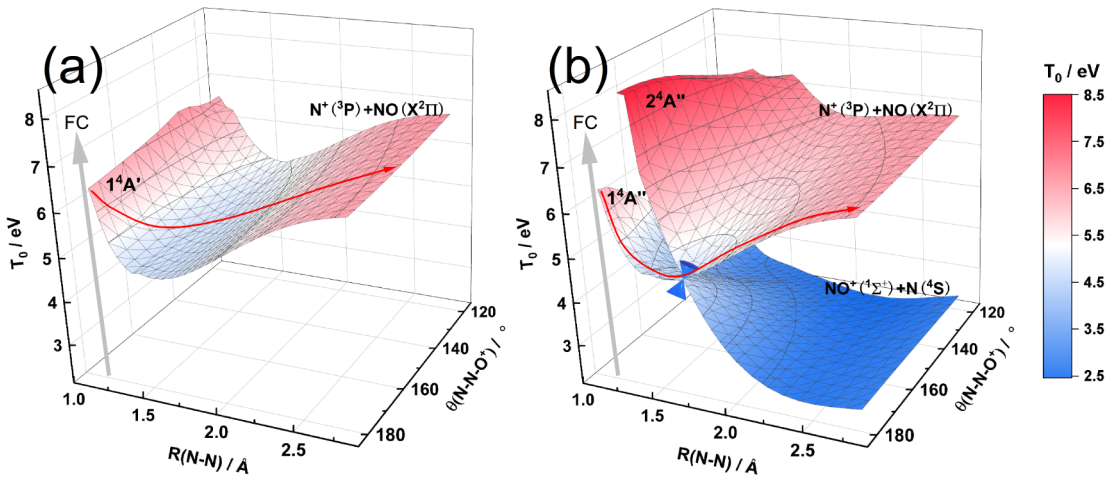

Figure 5. Two-dimensional multistate CASSCF potential energy surfaces of the three lowest quartet states for N_2O^+ along the N−NO and N−N−O coordinates, (a) $1^4A'$, (b) $1^4A''$ and $2^4A''$ states, in which the $1^4A'$ and $1^4A''$ states are split from the degenerate $1^4\Pi$ state in linear geometry. The thick gray arrows indicate the Franck−Condon regions of photoionization, and the red curves represent the feasible dissociation pathways used to produce the N^+ fragment.

the red arrow, a relatively lower barrier (∼1.0 eV) is located along the bending direction, and as the product, a local minimum (IM) with the R(N−NO) of ∼1.4 Å and θ(N−N−O) of ∼120° is formed and subsequently dissociates. The $N^+(^3P)$ and $NO(X^2\Pi)$ fragments are the adiabatic decomposition products of $C^2\Sigma^+$ in both linear or bent (C^2A') geometries as shown in Figure 4, providing an alternative and adiabatic pathway to form nitrogen atomic cation instead of the neutral atom.

However, such two high barriers can prevent the parent ions in low vibrational states from adiabatic decomposition. Consequently, the coupling from nearby electronic states is expected to cause the dissociation of $N_2O^+(C^2\Sigma^+)$ ions observed in experiments. We will discuss the corresponding mechanism in the following section.

3.5. N^+ Formation Mechanism from the N−NO Bond-Fission of $N_2O^+(C^2\Sigma^+)$. The NO^+ formation pathway of $N_2O^+(C^2\Sigma^+)$, as the dominant N−NO bond-fission channel, has been investigated previously,[11] in which the competition between the $NO^+(X^1\Sigma^+)$ + $N(^2D)$ and $NO^+(X^1\Sigma^+)$ + $N(^2P)$ pathways is thoroughly discussed with different vibrational excitations. Notably, the lowest dissociation channel, $NO^+(X^1\Sigma^+)$+ $N(^4S)$, has never been observed in experiments for the decomposition of $N_2O^+(C^2\Sigma^+)$.

In contrast, the N^+ formation must undergo an indirect process due to too high adiabatic barriers of $C^2\Sigma^+$. As indicated by the previous N-loss potential energy curves,[7] only the $1^4\Pi$ state adiabatically correlates with the dissociation limit of $N^+(^3P)$ + $NO(X^2\Pi)$ among all doublet and quartet states in the current photon energy range, while a slightly higher $1^4\Sigma^-$ state crosses the $1^4\Pi$ state and adiabatically correlates with the $NO^+(^1\Sigma^+)$ + $N(^4S)$ dissociation limit. Consequently, the spin−orbit coupling between the $C^2\Sigma^+$ and $1^4\Pi$ states should play a crucial role in the N^+ formation mechanism. Moreover, with a slightly linear-to-bent geometrical change prior to the N−NO bond rupture, the linear $1^4\Pi$ state can split into two substates of A′ and A″ symmetry. Notably, the avoided crossing between the $1^4A''(1^4\Pi)$ and $2^4A''(1^4\Sigma^-)$ states was not taken into account in the previous calculations[7] due to the linear geometry constraint. Therefore, in order to clarify the corresponding N^+ formation mechanism more comprehensively, 2D multistate CASSCF potential energy surfaces of the three lowest quartet states, $1^4A'(1^4\Pi)$, $1^4A''(1^4\Pi)$, and $2^4A''(1^4\Sigma^-)$, for N_2O^+ along the N−NO and angle coordinates were calculated and plotted in Figure 5.

As shown in Figure 5a, the potential energy surface of the $1^4A'(1^4\Pi)$ substate exhibits a typically bound-state characteristic in the N−NO coordinate and changes very slowly along the bond angle. This near-planar feature allows molecules to bend easily when adiabatically dissociating, corresponding to the expected bond angle χ of 151° using the "impulsive model". As a result, the rotationally excited NO neutral and the N^+ fragment are produced, providing a feasible mechanism to obtain the NO neutral fragment with rotational excitation.

In contrast, the potential energy surfaces of the electronic states in $^4A''$ symmetry are more complex. A conical intersection occurs between the $1^4A''(1^4\Pi)$ and $2^4A''(1^4\Sigma^-)$ states at the linear geometry of R(N−N) = 1.641 Å and R(N−O) = 1.148 Å, optimized at the coupled-perturbed CASSCF/cc-pVQZ level, as shown in Figure 5b. After passing through this interaction region, the $1^4A''$ state becomes repulsive and adiabatically correlates to the lowest dissociation limit of $NO^+(X^1\Sigma^+)$ + $N(^4S)$, while the upper $2^4A''$ state turns into a bound state with the adiabatic dissociation limit of $N^+(^3P)$ + $NO(X^2\Pi)$. Moreover, along the bending coordinate, the $1^4A''$ state is repulsive, while the $2^4A''$ state exhibits a trend of rapid potential growth. These features strongly imply that along the $1^4A''(1^4\Pi)$ potential energy surface, the N−NO bond fission should produce the $N^+(^3P)$ atomic ions and the $NO(X^2\Pi)$ fragment with low rotational excitation. In addition, this conical intersection actually provides a thermodynamically allowed charge-transfer pathway of $N^+ + NO \rightarrow N + NO^+$, when they approach ∼1.7 Å in a linear manner.

In summary, the $NO(X^2\Pi)$ and N^+ fragments can be produced by N−NO bond breaking via intersystem crossing (ISC) from $C^2\Sigma^+$ to $1^4\Pi$ in the Franck−Condon region. The "hot" rotational excitation of the NO fragment stems from adiabatic dissociation of the $1^4A'(1^4\Pi)$ substate in a slightly bent geometry, while the "cold" rotational component is attributed to the conical intersection between the $1^4A''(1^4\Pi)$ and $2^4A''(1^4\Sigma^-)$ states. These two N^+ formation pathways of $N_2O^+(C^2\Sigma^+)$ can be summarized as

https://doi.org/10.1021/acs.jpca.4c00494
J. Phys. Chem. A 2024, 128, 4439−4447

$$N_2O^+(C^2\Sigma^+) \xrightarrow{Spin-orbit\ couple} 1^4\Pi \rightarrow$$

$$\begin{cases} 1^4A' \xrightarrow{adiabatic\ dissociation} N^+(^3P) + NO(X^2\Pi), & \text{"hot" rotational} \quad (3) \\ 1^4A'' \xrightarrow{conicial\ intersection} 2^4A'' \rightarrow N^+(^3P) + NO(X^2\Pi), & \text{"cold" rotational} \quad (4) \end{cases}$$

3.6. The SOC Effect on the Vibrational-Dependent N^+ Formation from $N_2O^+(C^2\Sigma^+)$. Obviously, the spin−orbit coupling (SOC) between $C^2\Sigma^+$ and neighboring quartet states should play a decisive role in the decomposition of N_2O^+, especially when a slightly linear-to-bent geometric change occurs for parent ions. Given the large energy gap (1.61 eV) and the near-zero SOC value between the $C^2\Sigma^+$ and $2^4A''(1^4\Sigma^-)$ states in the Franck−Condon region, the ISC from $C^2\Sigma^+$ to $2^4A''(1^4\Sigma^-)$ can be excluded. Consequently, the SOC between the $C^2\Sigma^+$ and $1^4\Pi$ states is the unique candidate, which is calculated to be 8.6 cm^{-1} at the linear optimized geometry of $C^2\Sigma^+$, R(N−N) = 1.119 Å, and R(N−O) = 1.209 Å. Such a small SOC value agrees with the small branching ratio of N^+ observed in experiments, in comparison to the dominant decomposition channel of $NO^+(X^1\Sigma^+)$ + $N(^2D, ^2P)$.

As mentioned above, vibrational excitation exhibits significant influence on the energy and angular distributions of fragments in the decomposition of $N_2O^+(C^2\Sigma^+)$. As vibrational energies are almost negligible relative to the energy gaps between electronic states, the vibrational dependence could not be attributed to the effect of excitation energy. Accordingly, the influence of various vibrational modes on the SOC between the $C^2\Sigma^+$ and $1^4\Pi$ states might be the underlying cause since this interaction is the rate-controlling step in the overall unimolecular dissociation process. Hereby, harmonic frequency calculations and vibrational mode analyses were performed at the TDDFT-B3LYP/6-311G+(d) level. As listed in Table 4, the calculated vibrational frequencies of $N_2O^+(C^2\Sigma^+)$ are 1363 cm^{-1} for ν_1^+, 560 or 600 cm^{-1} for ν_2^+, and 2527 cm^{-1} for ν_3^+. Using the scaling factor of 0.93 for the calculated harmonic vibrational frequencies, these frequencies are in good agreement with the experimental data.[11]

Table 4. Vibrational Mode Analyses of N_2O^+ in the $C^2\Sigma^+$ State

modes	vibrational frequencies (cm^{-1})		relative weight (%)[c]		
	calc.[a]	expt.[b]	N−N stretching	N−O stretching	bending
ν_1^+	1363	1290,[11,19] 1274,[21] 1251[33]	33	67	-
ν_2^+	560/600	482[33]	-	-	100
ν_3^+	2527	2339,[11,19] 2371,[21] 2300[33]	56	(−)44	-

[a]Calculated at the TDDFT UB3LYP/6-311+G(d) level. [b]From references. [c](−) indicates that the stretching vibration phases of the N−N bond and the N−O bond are opposite.

As indicated by the vibrational mode analyses in Table 4, there are visible variations in the proportions of the N−O and N−N stretching components for the ν_1^+ and ν_3^+ modes. For the ν_1^+ mode, the N−O stretching is dominant at 67%. In contrast, the N−N and N−O bond lengths contribute almost equally in the ν_3^+ mode but in opposite phases. In other words, the increase of the N−N distance is accompanied by the reduced N−O distance when the ν_3^+ mode is excited.

To study how the vibrational modes affect the interaction between the $C^2\Sigma^+$ and $1^4\Pi$ states, the SOC values between $C^2A'(C^2\Sigma^+)$ and $1^4A'/1^4A''$ states were calculated as $\langle 1^4A'|H_{SO}|C^2A'\rangle$ and $\langle 1^4A''|H_{SO}|C^2A'\rangle$, respectively, with a slightly bent geometry (bond angle χ = 170°). Using the calculated relative weights for the ν_1^+ and ν_3^+ modes in Table 4, a few N−N and N−O bond lengths were used to represent the changing bond lengths due to vibrational excitations. For example, when the ν_1^+ mode is excited, the average N−N bond length is increased from 1.119 to 1.169 Å, and the N−O distance is also elongated from 1.209 to 1.310 Å. The calculated $\langle 1^4A'|H_{SO}|C^2A'\rangle$ and $\langle 1^4A''|H_{SO}|C^2A'\rangle$ values are equal to 11.7 and 13.0 cm^{-1}, respectively, and both of them are enhanced. Meanwhile, the energy gaps (ΔE) between $C^2A'(C^2\Sigma^+)$ and $1^4A'$, or $1^4A''$ are synchronously increased to 2.00 and 2.52 eV at the increased bond lengths. Based on the above N^+ formation mechanism, the branching ratio of the "hot" rotational component can be quantitatively determined by the ISC rate ratio along the "hot" and "cold" rotational fragmentation paths, where the ISC rate (k_{ISC}) can be expressed by

$$k_{ISC} = \frac{2\pi}{\hbar} |\langle 1^4\Pi|H_{so}|C^2\Sigma^+\rangle|^2 \cdot FCWD \quad (5)$$

with the Condon approximation, where FCWD stands for the Franck−Condon weighted density of final states at the $C^2A'(C^2\Sigma^+)$ energy.[40] Generally, the FCWD decreases exponentially with increasing ΔE within a low excitation energy range. Thus, formula 5 can be simplified as $k_{ISC} \propto |\langle 1^4\Pi|H_{so}|C^2\Sigma^+\rangle|^2 \cdot e^{-\Delta E/k_BT}$ in the current system. For the parallel decomposition of $N_2O^+(C^2\Sigma^+)$, the branching ratio of the "hot" rotational component via process (3) as $k_{ISC}(3)/[k_{ISC}(3) + k_{ISC}(4)]$ is increased from 0.50 at the $C^2\Sigma^+$ optimized geometry to 0.58 with the ν_1^+ excitation. The promoted contribution of the "hot" rotational component is generally consistent with the experimental results (in Table 1).

Likewise, the influence of the ν_3^+ mode on the branching ratio is discussed. In the ν_3^+ excitation, the average N−N bond length is increased to 1.169 Å, while the N−O distance is reduced to 1.170 Å, according to the calculated relative weights for the ν_3^+ mode (Table 4). At this geometry, $\langle 1^4A'|H_{SO}|C^2A'\rangle$ is decreased to 7.9 cm^{-1} while $\langle 1^4A''|H_{SO}|C^2A'\rangle$ is remarkably enhanced to 14.4 cm^{-1}. The two opposite trends correspond exactly to the significantly reduced branching ratio of the "hot" rotational component in the experiments. Therefore, the above semiquantitative estimates have amply confirmed the SOC effect on the vibration-dependent N^+ formation of $N_2O^+(C^2\Sigma^+)$ ions.

Last but not least, considering the $C^2\Sigma^+$ and $1^4\Pi$ states with unequal electronic structures, their intersection will cause the overlaps of Hermite functions with different numbers of vibrational quanta to not automatically integrate to zero, and the vibrational overlaps may be particularly large at the region close to the intersection. This strong coupling between electronic state and specific vibrational modes might be the reason for us to observe the mutations of vibrational populations in experiments. However, its precise calculation lies beyond our abilities using standard quantum chemical approaches.

4. CONCLUSIONS

In this work, using the TPEPICO velocity imaging and high-level quantum chemical calculations, we investigated the N^+ formation mechanism of N_2O^+ ions in vibrational state-selected $N_2O^+(C^2\Sigma^+)$ ions, e.g., (0,0,0), (1,0,0), and (0,0,1). The speed and angle distributions of fragments were derived

https://doi.org/10.1021/acs.jpca.4c00494
J. Phys. Chem. A 2024, 128, 4439−4447

from the TPEPICO 3D time-slice velocity images of N^+. Along the $N^+(^3P)$ + $NO(X^2\Pi)$ dissociation channel, low (J < 5) and high (J ∼ 24) rotational distributions of $NO(X^2\Pi)$ at each vibrational state were identified respectively. In contrast to the result at the (0,0,0) level, the formation of the high rotational component was promoted when the symmetric stretch ν_1^+ mode of $N_2O^+(C^2\Sigma^+)$ was excited, but the asymmetric stretching ν_3^+ mode showed the exact opposite influence. In particular, only "cold" rotational NO fragments were observed in the decomposition of N_2O^+ in the $C^2\Sigma^+(0,0,1)$ state.

To understand in-depth the N^+ formation mechanism, we have calculated 2D multistate potential energy surfaces of $C^2\Sigma^+$ and neighboring quartet states along the N−NO coordinate and bond angle at the CASSCF//cc-pVQZ level. Too high barriers for the $N^+(^3P)$ and $NO(X^2\Pi)$ products prevent the parent ions in low vibrational states from adiabatic decomposition. Thus, the intersystem crossing from $C^2\Sigma^+$ to $1^4\Pi$ becomes a unique feasible decomposition pathway for N^+ formation. In a slightly bent geometry, the spin−orbit coupling between $C^2\Sigma^+$ and $1^4A'(1^4\Pi)$ causes the production of the NO fragment with high rotational excitation. The formation of NO with "cold" rotational distribution undergoes a two-step process in sequence: the ISC from $C^2\Sigma^+$ and $1^4A''(1^4\Pi)$ followed by a conical intersection of $1^4A''(1^4\Pi)$ and $2^4A''(1^4\Sigma^-)$ in a linear manner. Notably, the conical intersection provides new insights into the charge-transfer reaction of $N^+ + NO \rightarrow N + NO^+$.

In addition, using a simple approximation, we quantitatively analyzed the influences of $N_2O^+(C^2\Sigma^+)$ vibrational modes on the SOC values between the $C^2\Sigma^+$ and $1^4\Pi$ states. The elongation of both N−N and N−O bond lengths in the excitation of ν_1^+ mode simultaneously enhances $\langle 1^4A'|H_{SO}|C^2A'\rangle$ and $\langle 1^4A''|H_{SO}|C^2A'\rangle$ values. However, due to the different ΔE between $C^2A'(C^2\Sigma^+)$ and $1^4A'$, or $1^4A''$, the contribution of "hot" rotational component is improved as a result, in line with the experimental conclusions. In contrast, when the ν_3^+ mode is excited, the increased $\langle 1^4A''|H_{SO}|C^2A'\rangle$ and the reduced $\langle 1^4A'|H_{SO}|C^2A'\rangle$ significantly promote the formation of NO with "cold" rotational distributions.

■ ASSOCIATED CONTENT

Supporting Information

The Supporting Information is available free of charge at https://pubs.acs.org/doi/10.1021/acs.jpca.4c00494.

Schematic and geometric diagrams of TPEPICO imaging spectrometer (Figure S1); threshold photoelectron spectrum for N_2O in the excitation energy range of 19.9−20.7 eV (Figure S2); the raw images and data processing using the time-sliced coincidence images of N^+ dissociated from $C^2\Sigma^+(0,0,0)$ state as a representative (Figure S3); angular distributions of the N^+ fragment dissociated from $N_2O^+(C^2\Sigma^+)$ ions in the (0,0,0) (Figure S4), (1,0,0) (Figure S5), and (0,0,1) (Figure S6) states; the parameters in curve fitting of three speed distributions of the N^+ fragment dissociated from $N_2O^+(C^2\Sigma^+)$ ions at the (0,0,0), (1,0,0), and (0,0,1) levels (Table S1) (PDF)

■ AUTHOR INFORMATION

Corresponding Authors

Xiaoguo Zhou − *Hefei National Research Center for Physical Sciences at the Microscale, Department of Chemical Physics, University of Science and Technology of China, Hefei 230026, China; Hefei National Laboratory, University of Science and Technology of China, Hefei 230088, China;* orcid.org/0000-0002-0264-0146; Email: xzhou@ustc.edu.cn

Xinhua Dai − *National Institute of Metrology, Beijing 100013, China;* orcid.org/0000-0002-0248-9554; Email: daixh@nim.ac.cn

Shilin Liu − *Hefei National Research Center for Physical Sciences at the Microscale, Department of Chemical Physics, University of Science and Technology of China, Hefei 230026, China; Hefei National Laboratory, University of Science and Technology of China, Hefei 230088, China;* orcid.org/0000-0002-3704-3798; Email: slliu@ustc.edu.cn

Authors

Yan Chen − *Hefei National Research Center for Physical Sciences at the Microscale, Department of Chemical Physics, University of Science and Technology of China, Hefei 230026, China*

Xiangkun Wu − *Hefei National Research Center for Physical Sciences at the Microscale, Department of Chemical Physics, University of Science and Technology of China, Hefei 230026, China;* orcid.org/0000-0001-8515-3302

Xinlang Yang − *Hefei National Research Center for Physical Sciences at the Microscale, Department of Chemical Physics, University of Science and Technology of China, Hefei 230026, China*

Complete contact information is available at: https://pubs.acs.org/10.1021/acs.jpca.4c00494

Notes

The authors declare no competing financial interest.

■ ACKNOWLEDGMENTS

The authors sincerely appreciate Prof. Xueming Yang for supporting our TPEPICO studies using synchrotron radiation and for encouraging us to carry out research combining FEL and PEPICO. The financial support of the National Key Research and Development Program of China (Nos. 2022YFF0707202 and 2016YFF0200502), the National Natural Science Foundation of China (No. 22073088), and the Innovation Program for Quantum Science and Technology (Nos. 2021ZD0303304 and 2021ZD0303102) are gratefully acknowledged. X.Z. and S.L. also thank the USTC-NSRL Association for funding supports. The quantum chemical calculations were performed on the supercomputing system in the Supercomputing Center of the University of Science and Technology of China.

■ REFERENCES

(1) Prather, M. J.; Hsu, J.; DeLuca, N. M.; Jackman, C. H.; Oman, L. D.; Douglass, A. R.; Fleming, E. L.; Strahan, S. E.; Steenrod, S. D.; Sovde, O. A.; et al. Measuring and Modeling the Lifetime of Nitrous Oxide Including Its Variability. *J. Geophys. Res.: atmos.* **2015**, *120*, 5693−5705.

(2) Jones, M. W.; Peters, G. P.; Gasser, T.; Andrew, R. M.; Schwingshackl, C.; Gütschow, J.; Houghton, R. A.; Friedlingstein, P.; Pongratz, J.; Le Quéré, C. National Contributions to Climate Change due to Historical Emissions of Carbon Dioxide, Methane, and Nitrous Oxide Since 1850. *Sci. Data* **2023**, *10*, 155.

(3) Tian, H. Q.; Xu, R. T.; Canadell, J. G.; Thompson, R. L.; Winiwarter, W.; Suntharalingam, P.; Davidson, E. A.; Ciais, P.;

Jackson, R. B.; Janssens-Maenhout, G.; et al. A Comprehensive Quantification of Global Nitrous Oxide Sources and Sinks. *Nature* **2020**, *586*, 248−256.
(4) Thompson, R. L.; Lassaletta, L.; Patra, P. K.; Wilson, C.; Wells, K. C.; Gressent, A.; Koffi, E. N.; Chipperfield, M. P.; Winiwarter, W.; Davidson, E. A.; et al. Acceleration of Global N2O Emissions Seen from Two Decades of Atmospheric Inversion. *Nat. Clim. Change* **2019**, *9*, 993−998.
(5) Ravishankara, A. R.; Daniel, J. S.; Portmann, R. W. Nitrous Oxide (N2O): The Dominant Ozone-depleting Substance Emitted in the 21st Century. *Science* **2009**, *326*, 123−125.
(6) Shuman, N. S.; Hunton, D. E.; Viggiano, A. A. Ambient and Modified Atmospheric Ion Chemistry: From Top to Bottom. *Chem. Rev.* **2015**, *115*, 4542−4570.
(7) Chambaud, G.; Gritli, H.; Rosmus, P.; Werner, H. J.; Knowles, P. J. The Ion−molecule Reaction O+(4S) + N2(X1Σ+) → NO+(X1Σ+, v′) + N(4S) and the Predissociation of the A2Σ+ and B2Π States of N2O+. *Mol. Phys.* **2000**, *98*, 1793−1802.
(8) Herburger, H.; Hollenstein, U.; Agner, J. A.; Merkt, F. PFI-ZEKE-Photoelectron Spectroscopy of N2O Using Narrow-band VUV Laser Radiation Generated by Four-wave Mixing in Ar Using a KBBF Crystal. *J. Chem. Phys.* **2019**, *151*, 144302.
(9) Zhou, Z.; Liang, H.; Hua, Z.; Feng, S.; Zhao, D.; Chen, Y. N-loss photodissociation dynamics of N2O+(B2Π) near the NO+(Σ+1) + N(2P) dissociation limit. *J. Chem. Phys.* **2019**, *150* (22), 226101.
(10) Tang, X. F.; Zhou, X. G.; Qiu, B. L.; Liu, S. L.; Liu, F. Y.; Shan, X. B.; Sheng, L. S. New Insight into Dissociative Photoionization of N2O at Similar to 20 eV Using Threshold Photoelectron-photoion Coincidence Velocity Imaging. *J. Electron Spectrosc. Relat. Phenom.* **2014**, *196*, 43−48.
(11) Tang, X.; Niu, M.; Zhou, X.; Liu, S.; Liu, F.; Shan, X.; Sheng, L. NO+ formation pathways in dissociation of N2O+ ions at the C2Σ+ state revealed from threshold photoelectron−photoion coincidence velocity imaging. *J. Chem. Phys.* **2011**, *134* (5), 054312.
(12) Meng, Q. Y.; Chang, H. B.; Huang, M. B.; Dong, H. Theoretical Studies on N-loss Predissociation Mechanisms of N2O +(A2Σ+) in Cs Symmetry. *Theor. Chem. Acc.* **2011**, *128*, 359−365.
(13) Wang, H.; Zhou, X.; Liu, S.; Jiang, B.; Dai, D.; Yang, X. Predissociation Dynamics of N2O+ at the AΣ2+ State: Three Pathways to Form NO+(Σ1+) Revealed from Ion Velocity Imaging. *J. Chem. Phys.* **2010**, *132*, 244309.
(14) Richard-Viard, M.; Atabek, O.; Dutuit, O.; Guyon, P. M. Experimental Evidence of Vibrational Mode Selectivity in the Indirect Predissociation of N2O+ A2Σ+. Energy Distribution of the Diatomic Fragment and Comparison with a Model Prediction. *J. Chem. Phys.* **1990**, *93*, 8881−8892.
(15) Gharaibeh, M. A.; Clouthier, D. J. A Laser-induced Fluorescence Study of the Jet-cooled Nitrous Oxide Cation (N2O +). *J. Chem. Phys.* **2012**, *136*, 044318.
(16) Lebech, M.; Houver, J. C.; Dowek, D.; Lucchese, R. R. Dissociative Photoionization of N2O in the Region of the N2O +(B2Π) State Studied by Ion−electron Velocity Vector Correlation. *J. Chem. Phys.* **2004**, *120*, 8226−8240.
(17) Chen, Y.; Wu, X. K.; Yu, T. P.; Zhou, X. G.; Yan, B.; Liu, S. L. Theoretical Re-investigation on the N-N Bond Breaking of N2O+ Cations in the A2Σ+ and B2Π States at the CASPT2 Level. *Chem. Phys. Lett.* **2023**, *831*, 140857.
(18) Lorquet, J. C.; Cadet, C. Excited States of Gaseous Ions: I. Selection Rules in Photoelectron Spectroscopy and Photoionization. The Case of N2O+. *Int. J. Mass Spectrom.* **1971**, *7*, 245−254.
(19) Nenner, I.; Guyon, P. M.; Baer, T.; Govers, T. R. A Threshold Photoelectron−photoion Coincidence Study of the N2O+ Dissociation Between 15 and 20.5 eV. *J. Chem. Phys.* **1980**, *72*, 6587−6592.
(20) Kinmond, E.; Eland, J. H. D.; Karlsson, L. Dissociation of N2O + Ions from the Valence States Reached by One-photon Photoionisation11Dedicated to Professor Michael T. Bowers on the Occasion of His 60th Birthday. *Int. J. Mass Spectrom.* **1999**, *185*−*187*, 437−447.
(21) Chiang, S.-Y.; Ma, C.-I. Fragmentation of Vibrationally Selected N2O+ in State C2Σ+ from Measurements of Threshold Photoelectron Photoion Coincidence. *J. Phys. Chem. A* **2000**, *104*, 1991−1996.
(22) Lebech, M.; Houver, J. C.; Dowek, D.; Lucchese, R. R. Dissociative Photoionization of N2O in the Region of the N2O +(B2Π) State, Studied by Ion−electron Velocity Vector Correlation. *J. Chem. Phys.* **2002**, *117*, 9248−9257.
(23) Berkowitz, J.; Eland, J. H. D. Photoionization of N2O: Mechanisms of Photoionization and Ion Dissociation. *J. Chem. Phys.* **1977**, *67*, 2740−2752.
(24) Ng, C.-Y.; Baer, T.; Powis, I. *Unimolecular and bimolecular ion−molecule reaction dynamics*; Wiley, 1994.
(25) Midey, A. J.; Miller, T. M.; Viggiano, A. A. Reactions of N+, N2+, and N3+ with NO from 300 to 1400 K. *J. Chem. Phys* **2004**, *121*, 6822−6829.
(26) *Active Thermochemical Tables (ATcT) Values Based on Ver. 1.122p of the Thermochemical Network*; http://ATcT.anl.gov, 2020.
(27) Wu, X. K.; Tang, X. F.; Zhou, X. G.; Liu, S. L. Dissociation Dynamics of Energy-selected Ions Using Threshold Photoelectron-photoion Coincidence Velocity Imaging. *Chin. J. Chem. Phys.* **2019**, *32*, 11−22.
(28) Tang, X.; Zhou, X.; Niu, M.; Liu, S.; Sun, J.; Shan, X.; Liu, F.; Sheng, L. A Threshold Photoelectron-photoion Coincidence Spectrometer with Double Velocity Imaging Using Synchrotron Radiation. *Rev. Sci. Instrum.* **2009**, *80*, 113101.
(29) Wang, S.; Kong, R.; Shan, X.; Zhang, Y.; Sheng, L.; Wang, Z.; Hao, L.; Zhou, S. Performance of the Atomic and Molecular Physics Beamline at the National Synchrotron Radiation Laboratory. *J. Synchrotron Radiat.* **2006**, *13*, 415−420.
(30) Bodi, A.; Sztaray, B.; Baer, T.; Johnson, M.; Gerber, T. Data Acquisition Schemes for Continuous Two-particle Time-of-flight Coincidence Experiments. *Rev. Sci. Instrum.* **2007**, *78*, 084102.
(31) Werner, H.-J.; Knowles, P. J.; Knizia, G.; Manby, F. R.; Schuetz, M. *MOLPRO, Version 2021.3, A Package of Ab Initio Programs*, 2021. https://www.molpro.net.
(32) Frisch, M. J.; Trucks, G. W.; Schlegel, H. B.; Scuseria, G. E.; Robb, M. A.; Cheeseman, J. R.; Scalmani, G.; Barone, V.; Petersson, G. A. *Gaussian 16 Revision C.01*; Gaussian, Inc: Wallingford CT, 2016. https://gaussian.com.
(33) Chen, W.; Liu, J.; Ng, C. Y. Vacuum Ultraviolet Pulsed Field Ionization−Photoelectron Study for N2O+ in the Energy Range of 16.3-21.0 eV. *J. Phys. Chem. A* **2003**, *107*, 8086−8091.
(34) Tang, X.; Zhou, X.; Niu, M.; Liu, S.; Sheng, L. Dissociation of Vibrational State-Selected O2+ Ions in the B2Σg⁻ State Using Threshold Photoelectron−Photoion Coincidence Velocity Imaging. *J. Phys. Chem. A* **2011**, *115*, 6339−6346.
(35) Herzberg, G. *Molecular Spectra and Molecular Structure*; Spectra of Diatomic Molecules; 1950, Vol. *1*.
(36) Laane, J.; Ohlsen J, R. *Progress in Inorganic Chemistry*; Wiley, 1980.
(37) Johns, J. W. C.; Reid, J.; Lepard, D. W. Vibration-Rotation Fundamentalof of NO. *J. Mol. Spectrosc.* **1977**, *65*, 155−162.
(38) Busch, G. E.; Wilson, K. R. Triatomic Photofragment Spectra.1. Energy Partitioning in NO2 Photodissociation. *J. Chem. Phys.* **1972**, *56*, 3626−3638.
(39) Zare, R. N. Photoejection dynamics. *Mol. Photochem.* **1972**, *4*, 1−37.
(40) Marian, C. M. Understanding and Controlling Intersystem Crossing in Molecules. *Annu. Rev. Phys. Chem.* **2021**, *72*, 617−640.

https://doi.org/10.1021/acs.jpca.4c00494
J. Phys. Chem. A 2024, 128, 4439−4447